Moiré superstructures in marginally twisted $NbSe_2$ bilayers

James G. McHugh,[1,2] Vladimir V. Enaldiev,[1,2] and Vladimir I. Fal'ko[1,2,3]
[1]*School of Physics and Astronomy, University of Manchester, Manchester M13 9PL, United Kingdom*
[2]*National Graphene Institute, University of Manchester, Manchester M13 9PL, United Kingdom*
[3]*Henry Royce Institute, University of Manchester, Manchester M13 9PL, United Kingdom*

(Received 2 June 2023; revised 9 October 2023; accepted 1 December 2023; published 26 December 2023)

The creation of moiré superlattices in twisted bilayers of two-dimensional crystals has been utilized to engineer quantum material properties in graphene and transition metal dichalcogenide semiconductors. Here, we examine the structural relaxation and electronic properties in small-angle twisted bilayers of metallic $NbSe_2$. Reconstruction appears to be particularly strong for misalignment angles $\theta_P < 2.9^\circ$ and $\theta_{AP} < 1.2^\circ$ for parallel (P) and antiparallel (AP) orientations of monolayers' unit cells, respectively. Multiscale modeling reveals the formation of domains and domain walls with distinct stacking, for which density functional theory calculations are used to map the shape of the bilayer Fermi surface and the relative phase of the charge density wave (CDW) order in adjacent layers. We find a significant modulation of interlayer coupling across the moiré superstructure and the existence of preferred interlayer orientations of the CDW phase, necessitating the nucleation of CDW discommensurations at superlattice domain walls.

DOI: 10.1103/PhysRevB.108.224111

Introduction. The field of twistronics, where a relative twist is applied between adjacent layers in two-dimensional crystalline structures, has recently emerged as a promising method to control electronic [1,2] and structural [3–12] properties. For example, in semiconducting transition metal dichalcogenides (TMDs), with chemical formula MX_2 (M = Mo, W; X = S, Se), it has recently been established that the moiré pattern in twisted bilayers undergoes significant reconstruction [4–6,13] at marginal (i.e., sufficiently small) twist angles.

The niobium (or tantalum) atoms of metallic TMDs host one fewer d electron in the valence shell. The chemical potential then lies in the valence band, in contrast to semiconducting TMDs, allowing superconducting and charge density wave (CDW) phases in monolayers and bulk [14–19]. Here, interlayer effects are also found to be important, moderating the critical temperatures of the superconducting [20,21] and CDW [22,23] transitions, enabling van der Waals Josephson junctions through interlayer twisting [24,25] and leading to spatial variation of the Gibbs free energy of hydrogen absorption [26]. Despite these fascinating properties, there have been no detailed theoretical studies of the structural relaxation of twisted bilayers of metallic TMDs and the consequent effect of stacking on electronic properties. Here we address these questions for twisted bilayers of $NbSe_2$ using *ab initio* density functional theory (DFT) modeling combined with multiscale analysis of lattice relaxation.

Ab initio analysis of adhesion energy. DFT calculations were performed as implemented in the QUANTUM ESPRESSO code [27,28]. Core electrons were approximated using Vanderbilt ultrasoft pseudopotentials [29] under the generalized gradient approximation (GGA), as parametrized by Perdew, Burke, and Ernzerhof [30]. A plane-wave cutoff of $E_w = 50$ Ry and charge density cutoff of $E_\rho = 600$ Ry were applied. A Monkhorst-Pack k-point grid of dimensions $15\times15\times1$ [31] and Fermi-Dirac smearing of width $\sigma = 0.01$ eV are applied to aid convergence. Interlayer dispersion is implemented through the optB88-vdW functional [32–35]. Band structure calculations were performed using $E_w = 80$ Ry and a $21\times21\times1$ k-point grid. In both band structure and adhesion parametrization calculations, we fix the in-plane lattice constant to the DFT-calculated bulk value, while interlayer distance is optimized for each stacking configuration.

To assess the preferred stacking order, bilayers of $NbSe_2$ were structurally relaxed in a variety of stacking configurations illustrated by sketches in Fig. 1(a). Bilayer structures are divided into two classes: antiparallel (AP), where a 180° rotation of the top layer restores centrosymmetry, which is absent in a monolayer, and parallel (P), where monolayers have the same orientation and centrosymmetry is absent. Comparison of different stackings shows that the lowest-energy stacking polymorph is the metal-overlapping, MM (also called $2H_a$ [36,37]) configuration [see Fig. 1(b)]. Full structural optimization of the bulk structure yields lattice constants $a = 3.45$ Å and $c = 12.74$ Å [38] and elastic moduli (see Appendix A 2) which are in good agreement with available experimental values [38–40]. $2H$ stacking, which is preferred for semiconducting TMDs, is reasonably close in energy. While it has been found with a smaller areal density in $NbSe_2$ bilayers grown using chemical vapor deposition (CVD) [41], it is a metastable state, whereas the MM configuration is the most common and is thermodynamically stable. We note that the bulk structure of $NbSe_2$ has frequently been referred to (and

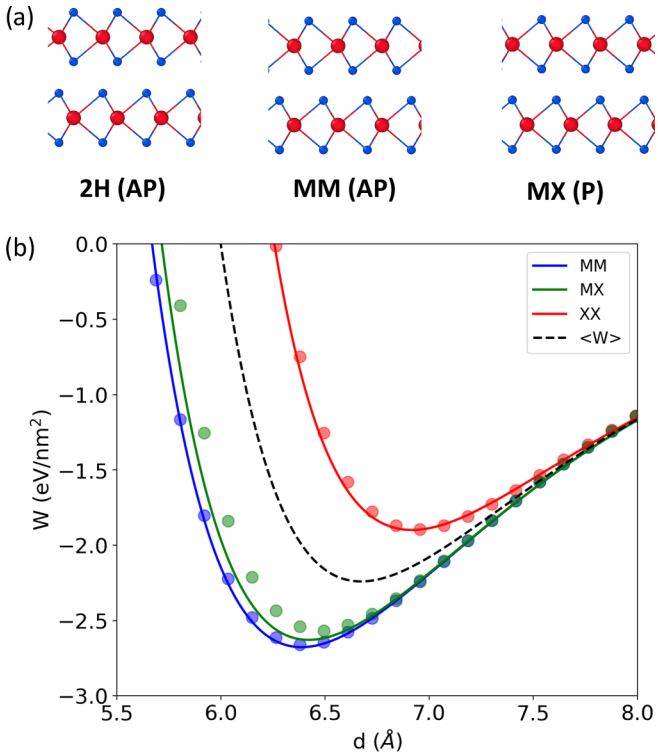

FIG. 1. (a) Side view of antiparallel $2H$ stacking, antiparallel MM stacking, and parallel MX stacking orders of $NbSe_2$ bilayers. Additional stacking configurations are shown in Appendix A 1. (b) Adhesion energy vs interlayer separation for MM, MX, XX, and $\langle W\rangle$ (configuration-averaged) stacking configurations.

sometimes even modeled) as $2H$ stacking [42–45]; therefore, to avoid confusion, below we employ the nomenclature of relevant stacking configurations as shown in Fig. 1.

In twisted bilayers, moiré superlattice reconstruction is fully determined by the stacking-dependent variation of adhesion energy between the constituent layers. Following the approach of Ref. [46], we employ an interpolation formula to fit the adhesion energy as a function of local disregistry $\boldsymbol{r}_0$. This is parametrized in a coordinate system where XX stacking corresponds to zero displacement, i.e., $\boldsymbol{r}_0 = (0, 0)$, and interlayer distance d:

$$W(\boldsymbol{r}_0, d) = f(d) + A_1 e^{-(d-d_0)\sqrt{G^2+\rho_1^{-2}}} \cos(\boldsymbol{G}_n \boldsymbol{r}_0) + A_2 e^{-(d-d_0)\sqrt{G^2+\rho_2^{-2}}} \sin(\boldsymbol{G}_n \boldsymbol{r}_0 + \phi_{\mathrm{P(AP)}}). \quad (1)$$

Here, $f(d) = C_3/d^{12} + C_2/d^8 - C_1/d^4$ is the stacking-averaged adhesion energy, characterizing long-distance van der Waals attraction between the layers ($\propto -1/d^4$) and short-distance repulsion ($\propto 1/d^{12}$), $\boldsymbol{G}_n$ are reciprocal lattice vectors, and A_i and ρ_i are fit parameters. The phases $\phi_{\mathrm{P}} = 0$ and $\phi_{\mathrm{AP}} = \pi/2$ distinguish P and AP unit cell orientations, reflecting the symmetry of these alignments.

Fitting to DFT results leads to optimal interlayer distances $d_0 = 0.66$ nm and $d_* = 0.65$ nm for configuration-averaged and ground (MM) stackings, respectively. Expanding Eq. (1) around d_* for $\boldsymbol{r}_0^{MM} = (0, -2a/\sqrt{3})$ [$W \approx W_{\min} + \epsilon_*(d - d_*)^2$, $\epsilon_* \approx 257$ eV/nm^4] allows us to estimate the frequency of the layer breathing mode in MM-stacked $NbSe_2$ bilayers as follows: $\omega_{\mathrm{BM}} = \sqrt{4\epsilon_* S_{\mathrm{uc}}/\mu} \approx 33.8$ cm^{-1} (4.2 meV). Here, μ and S_{uc} are the mass and area of the $NbSe_2$ monolayer unit cell, respectively. The computed value is in a good agreement with the experimental value $\omega_{\mathrm{BM}} \approx 34$ cm^{-1} [47], which validates the DFT-fitted shape of the adhesion energy (1) around d_*.

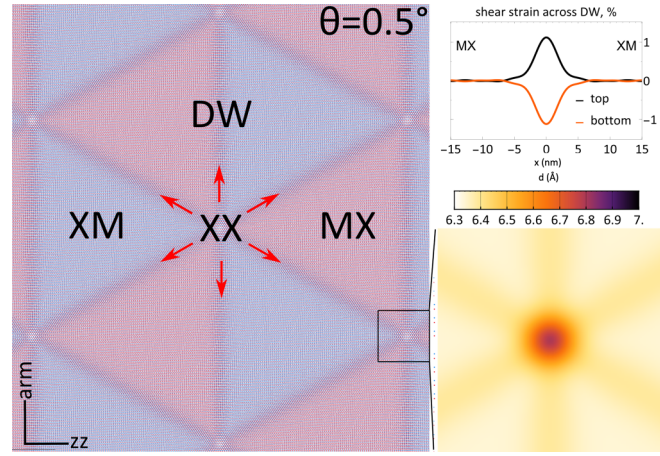

FIG. 2. Left: reconstructed moiré superlattice in P-$NbSe_2$ bilayers at $\theta = 0.5°$. Red arrows show the directions of Burgers vectors characterizing the shift of the atomic register across domain walls. Top right: we demonstrate distribution of the only nonzero shear strain across a single domain wall. The inset at bottom right shows a map of the interlayer distance around the XX area given by $d(\boldsymbol{r}_0(\boldsymbol{r}))$.

Lattice reconstruction in twisted $NbSe_2$ *bilayers.* The lattice of twisted $NbSe_2$ bilayers is modeled using a multiscale approach implemented earlier in Ref. [46] for the analysis of semiconducting TMDs. This incorporates the microscopic expression for adhesion energy (1) and elasticity theory applied to the mesoscale strains across a long-period moiré superlattice, which reduces to minimization of total (adhesion and elastic) energy over the moiré supercell. In the elastic energy, characterized by elastic moduli λ and μ, we take into account only in-plane strains in the top (t) and bottom (b) layers, $U = \sum_{l=t,b}[(\lambda/2)(u_{ii}^{(l)})^2 + \mu u_{ij}^{(l)} u_{ji}^{(l)}]$, neglecting minor bending energies of layers (see Supplemental Material of Ref. [46]) due to adjustment of the local optimal interlayer distance with corresponding stacking across the moiré superlattice. To find the latter, we expand $f(d)$ around its extremum $[f(d_0) + \varepsilon(d - d_0)^2]$, we also expand the exponential terms in (1) up to linear order in $d - d_0$, and then minimize the resulting expression as a function of d, to obtain an expression for the optimal interlayer distance for every stacking, $d(\boldsymbol{r}_0)$. Here, $\boldsymbol{r}_0(\boldsymbol{r}) = \theta \hat{z} \times \boldsymbol{r} + \boldsymbol{u}_t - \boldsymbol{u}_b$, where the first term describes the contribution of geometrical twist between the layers and where in-plane displacements $\boldsymbol{u}_t$ and $\boldsymbol{u}_b$, responsible for local deformations in the t and b layers, respectively, are found from minimization to the total energy.

In Fig. 2 we display the reconstructed moiré superlattice resulting from minimization of the total energy in twisted $NbSe_2$ bilayers. Similarly to semiconducting TMDs, at $\theta \leqslant \theta_{\mathrm{P}}^* \approx 2.9°$ [48] this results in the formation of arrays of triangular domains with rhombohedral stacking (XM and MX), separated by a domain wall (DW) network. Each domain wall

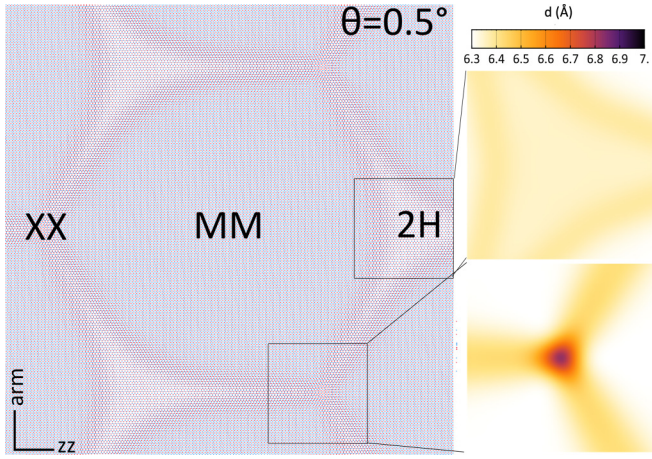

FIG. 3. Reconstructed moiré superlattice in AP-$NbSe_2$ bilayers at $\theta = 0.5^\circ$. The upper (lower) inset shows an interlayer distance map around the $2H$ (XX) stacking area.

in the network is a partial screw dislocation with dominating shear strain and a Burgers vector length $a/\sqrt{3}$, shown by red arrows for several DWs merging into a DW network node. The magnitude of shear strain reaches 1% in the middle of the domain wall; see the top right panel of Fig. 2.

For AP-$NbSe_2$ bilayers with $\theta \leqslant \theta^*_{AP} \approx 1.2^\circ$ (Fig. 3), lattice reconstruction leads to the expansion of the lowest-energy MM domains and the formation of a hexagonal superlattice domain wall network. The other high-symmetry ($2H$ and XX) stackings occupy corners of the domains, linked by perfect screw dislocations, characterized by a stacking shift of a single translation vector along zigzag axes. We note that the critical angles θ^*_P and θ^*_{AP} are slightly higher than those for semiconducting TMDs [46] because of the softer $NbSe_2$ lattice.

TABLE I. Fitted parameters of monolayer $NbSe_2$ bands calculated at the Fermi level (values in parentheses are calculated close to the center of the pocket). E_0 is the pocket depth, $m^* = m/m_e$ is the electron effective mass, $C_{3(6)}$ accounts for trigonal (hexagonal) warping at the K (Γ) pocket, and λ_{SOC} is the magnitude of the SOC.

Pocket	E_0	m^*	$C_{3(6)}$ (eVÅ^3)	λ_{SOC} (meV)
Γ	0.61	−2.42 (−2.97)	1.29 (0.37)	35 (35)
K	0.63	−0.79 (−0.59)	3.41 (13.50)	55 (67)

Electronic structure. The Fermi surface of an $NbSe_2$ monolayer is shown in Fig. 4(a). There are three distinct hole pockets across the Brillouin zone (BZ): one Γ-centered pocket and a pair of triangular $K_\pm$ pockets. The dispersion around each pocket ($i = \Gamma/K_\pm$) is

$$\epsilon_i(\boldsymbol{p}) = E_{0,i} + \frac{\hbar^2 \boldsymbol{p}^2}{2m_i^*} + C_i|\boldsymbol{p}^3|\cos(3\phi) + \beta_i\sigma_z, \qquad (2)$$

where $\boldsymbol{p} = \boldsymbol{k} - \boldsymbol{K}_i$ is the Bloch state momentum relative to the pocket center, m_i^* is the effective mass, C_i parameters account for trigonal and hexagonal warping, σ_z is a Pauli matrix operating on spin, $\phi =$ arctan(k_y/k_x) [49], and $E_{0,i}$ is the energy difference between the band edge and the Fermi level. The shape of the metallic band is overall extremely similar to the conduction band in semiconducting TMDs, with similar effective masses m_i^* and a high degree of trigonal warping around the K pockets (see Table I) [16]. Significant Ising spin-orbit coupling (SOC) is evident across the BZ, with splitting $\propto \beta(k)\sigma_z$. A map of $\beta(k)$ across the entire BZ is displayed in Fig. 4(a), with a maximum value of 78 meV deep in the $K_\pm$ pockets. In the Γ pocket, SOC vanishes along the Γ-M lines, $\beta_\Gamma = \lambda_\Gamma|p|^3\cos(3\phi)$, while it is approximately constant, $\beta_K = \pm\lambda_K$, in the $K_\pm$ pockets [50].

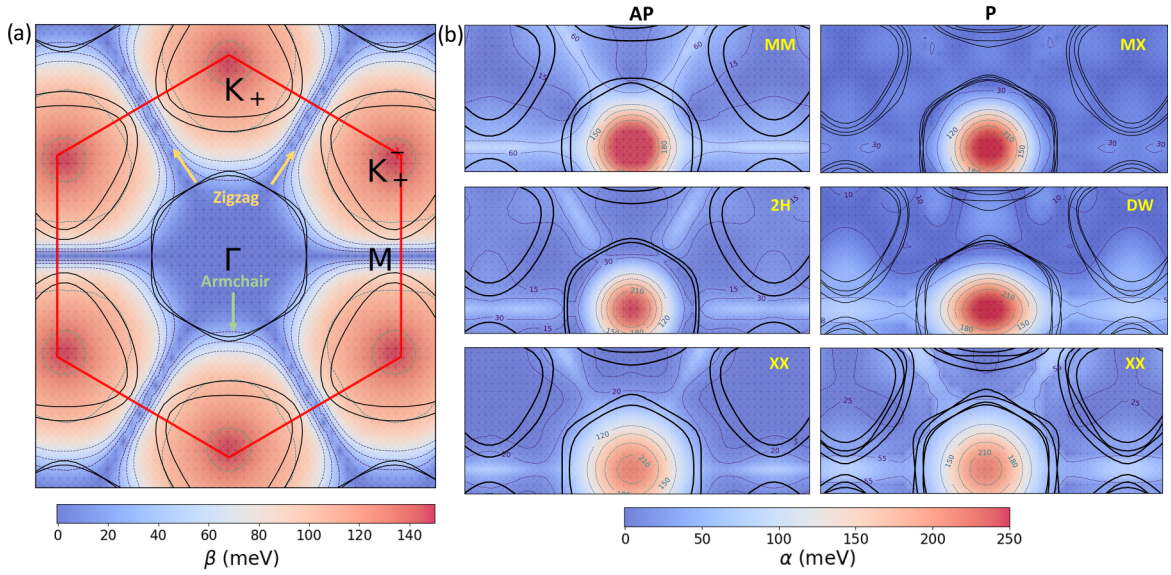

FIG. 4. (a) Two-dimensional Fermi lines for an $NbSe_2$ monolayer. The color overlay maps the magnitude of the spin-orbit splitting. The maximum magnitude of band splitting from spin-orbit effects only is ≈156 meV ($\beta = 78$ meV). (b) Bilayer Fermi lines and magnitude of interlayer-hybridization parameter $\alpha(\mathbf{k})$ in selected stacking configurations. Splitting around $K_\pm$ pockets is determined by SOC effects, while Γ pocket splitting is largely due to interlayer interactions. DW corresponds to the P-bilayer "MX-XM" structure in Appendix A 1.

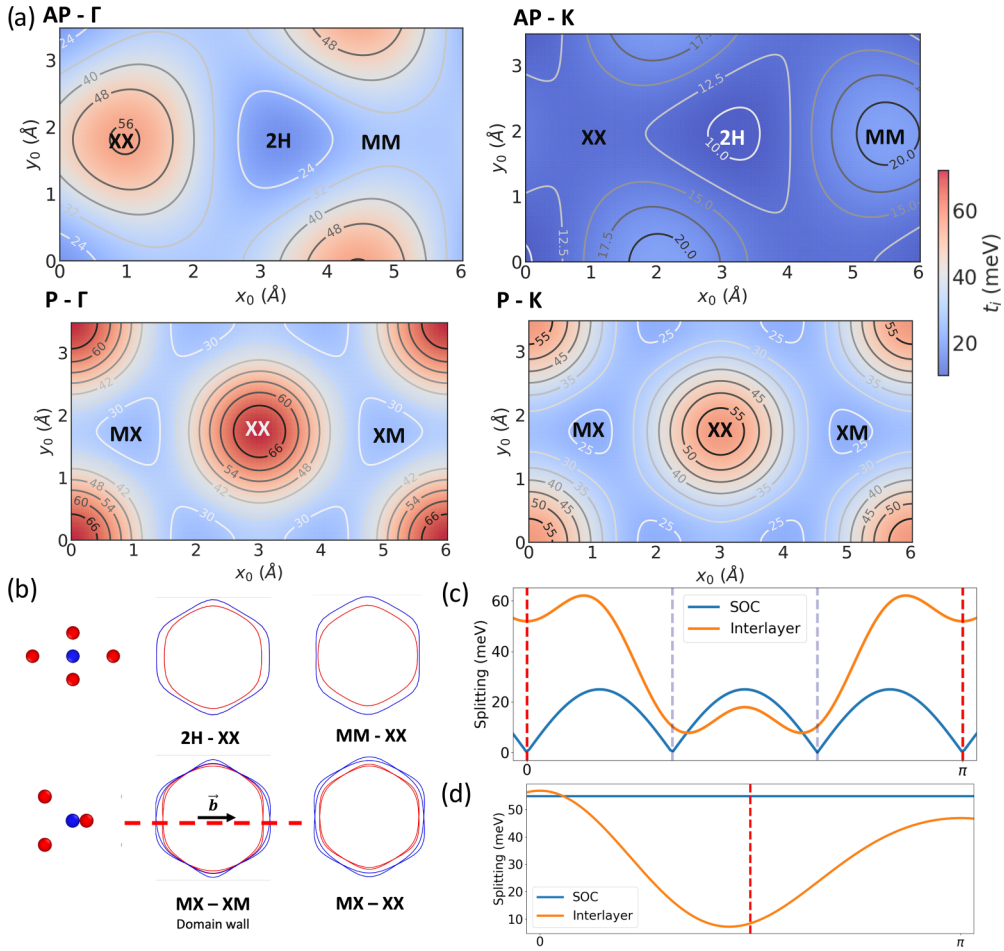

FIG. 5. (a) DFT-calculated variation of the average interlayer hopping parameter $\bar{t}_i$ with disregistry, calculated by averaging the splitting at the Fermi level along six distinct crystallographic directions. Energy values are in meV. (b) Modulation of the shape of the Γ-pocket Fermi lines for different intermediate stacking configurations in AP and P bilayers, and corresponding interlayer orientation of Nb atoms. (c) and (d) Variation in the magnitude of the spin-orbit and interlayer contributions vs angular orientation relative to the pocket center, for the Γ (c) and K pockets (d) at a domain wall in a P bilayer, extracted from DFT calculations.

Stacking modulation of interlayer hybridization results in variation of the electronic Fermi surface around each pocket. To quantify this, we relate DFT-calculated energy eigenvalues across the entire BZ to a momentum-dependent hybridization parameter $\alpha(k)$, assuming a simple layer-hybridized wave function, $\Psi(k) = (\psi_1(k) \pm \psi_2(k))\sqrt{2}$, with energies $E_{\mathrm{ML}}(k) \pm \alpha(k)$, where $E_{\mathrm{ML}}(k)$ are monolayer energy eigenvalues [51].

Plots of this parameter calculated across the BZ are overlaid with the DFT-calculated Fermi surface in Fig. 4(b). We observe that in centrosymmetric AP configurations, interlayer hybridization leads to a pair of spin-layer locked, layer-hybridized bands which cross the Fermi level in all stacking configurations. In contrast, broken centrosymmetry of the P bilayers leads to four Fermi lines, which are essentially a pair of layer-hybridized copies of the monolayer bands. DFT calculations in mirror-reflected supercells also demonstrate the presence of a ferroelectric charge transfer, resulting in an ≈ 11 meV potential energy drop between the layers (see Appendix A 3), which is notably smaller than for semiconducting TMDs [52]. We note that this charge transfer in principle allows for a layer-dependent potential contribution to interlayer band splitting of P bilayers; however, explicit incorporation of this term does not have a significant effect on interlayer hybridization due to the small degree of charge transfer between the layers (see comparison between Fermi surface fitting with and without an explicit layer-polarization term in Appendix A 4).

In both bilayer orientations, there is a substantial sixfold (threefold) modulation of the hybridization parameter around the Γ ($K_\pm$) pockets, as shown in Fig. 4(b) (see also Appendix A 5). This modulation is proportional to the out-of-plane d_z^2-orbital component, leading to maxima along the Γ-M and K-M lines around each pocket. The resulting interlayer hybridization, and the associated shape of the Fermi lines, is moderated by the interlayer coordination of Nb atoms. Consequently, there are also distinct modulations of the interlayer hybridization at domain walls, which is evident as a twofold "squeezing," of both the Γ and K pockets, along distinguished directions of the Brillouin zone for the intermediate stacking configurations occurring at domain walls [see Fig. 4(b), P-DW]. For example, at the domain walls of a P-oriented moiré superlattice we find that there is significantly stronger hybridization of Γ-pocket electrons with

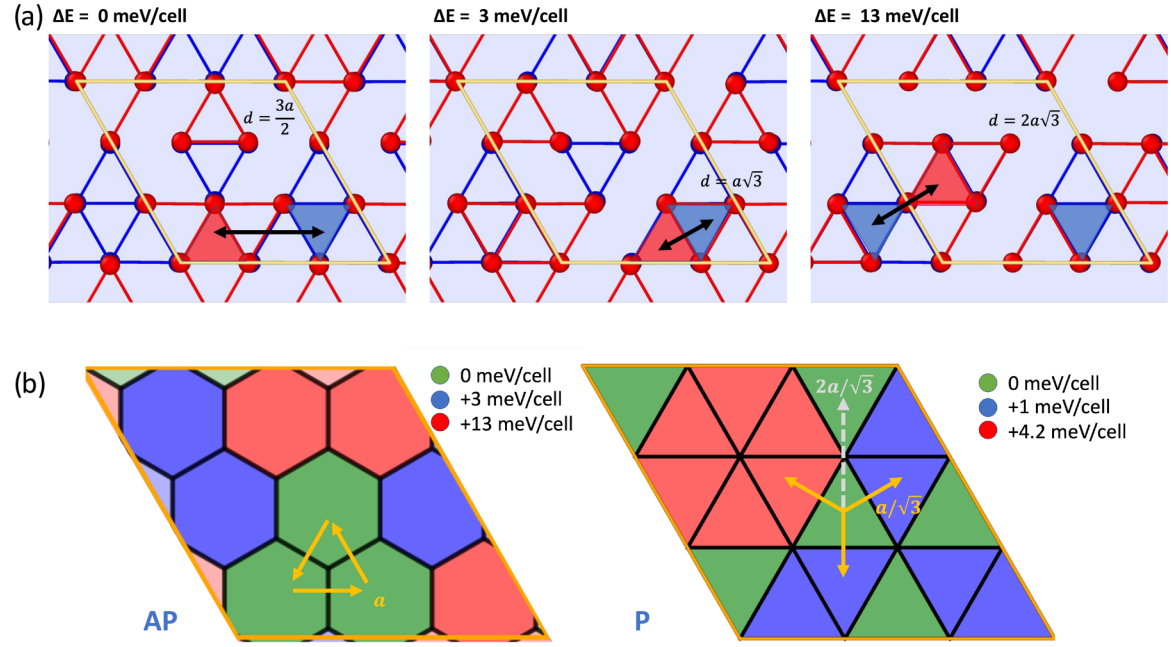

FIG. 6. (a) DFT-relaxed bilayer structures with different interlayer offsets of the CDW order between layers. For clarity, only the Nb sublattice is shown in red (blue) for the top (bottom) layer, and the center of the CDW distortion is marked as the center of the "large" triangle in each layer. (b) Energy of the CDW phase, relative to the most favorable configuration, at different orientations of an AP bilayer (left) and a P bilayer (right), in units of meV/unit cell.

crystal momenta parallel to the dislocation line compared with the perpendicular direction, while the opposite is the case for the K pocket. A comparison of the degree of asymmetric warping, and the corresponding positions of Nb atoms in both layers, is shown in Fig. 5(b) for various intermediate stacking configurations of P and AP bilayers, which demonstrates qualitatively similar distortion between the two bilayers as a function of Nb-interlayer offset. Furthermore, we note that in both pockets the degree of interlayer coupling can be lifted below or above that of the spin-orbit term, depending on the pocket index and crystal momentum [see Figs. 5(c) and 5(d)].

Using DFT data, we quantify the effective interlayer hopping around each pocket by introducing an extra index which acts in layer space. This is encoded in a bilayer Hamiltonian,

$$\mathcal{H}(\mathbf{p}) = \sum_i d^\dagger_{i,\mathbf{p},s,l}\left[\epsilon_i(\mathbf{p})\sigma_0\eta_0 + \alpha_i(\mathbf{p})\sigma_0\eta_x + \beta_i(\mathbf{p})\sigma_z^a\eta_0\right]d_{i,\mathbf{p},s,l}, \tag{3}$$

where $d^\dagger$ (d) is the electron creation (annihilation) operator, i is the pocket index, $\boldsymbol{p}$ is the Bloch state momentum relative to the pocket center, and s and l are spin and layer indices. $\eta_{x,0}$ are Pauli matrices operating on the layer index, where the parameter $a = 1, 2$ for AP and P bilayers, respectively, and α_i is the strength of hybridization around the corresponding pocket, where modulation is accounted for using appropriate periodic terms in α_i. The hybridization term then takes the form

$$\alpha_i(p) = \bar{t}_i + \sum_n t_{i,n}\cos(n\phi), \tag{4}$$

where $\bar{t}_i$ is the average hybridization around the pocket. We find that hybridization is approximately constant for momenta $p \approx |p_F|$, with angular variation $\propto \phi$ incorporated via $\bar{t}_{i,n}$ periodic terms. Further details of these terms in high-symmetry stackings are given in Appendixes A 6 and A 7.

To facilitate a simple comparison between different domains in the moiré superstructure, we analyze the average interlayer hopping $\bar{t}_i$ [the first term in Eq. (4)] at each pocket as a function of interlayer disregistry. We numerically extract this parameter from DFT calculations by averaging interlayer splitting around each pocket along the high-symmetry directions (Γ-M, Γ-K, K-M, and K-Γ). This procedure was repeated for relaxed bilayers with different interlayer offsets, and the extracted value of $\bar{t}_i$ was found to fit to an expansion using only the first star of reciprocal lattice vectors with reasonable accuracy (see Appendixes A 8 and A 9). Figure 5(a) shows this expansion for both pockets in AP and P bilayers.

Interestingly, we find distinct variation of interlayer hybridization between the Γ and K pockets in AP bilayers. For the former, which is most sensitive to the interlayer distance between Se atoms, it is maximal at XX corners, while interlayer hybridization at the K pocket is strongest inside the lowest-energy MM domains. Interactions are weakest at the $2H$ corners for both pockets. An opposite trend was found for the moiré superlattice of a P bilayer. In this case, the interlayer separation of chalcogen atoms is rather larger within domains due to trigonal interlayer coordination, and there are correspondingly weaker interlayer interactions, which become larger at corners and domain walls where the interlayer Se distance is reduced. The overall variation is qualitatively similar at both pockets.

CDW modulation. Lastly, we examine the ability of the reconstructed moiré superlattice to impact the relative phase of the CDW distortion in adjacent layers, as a function of

the interlayer disregistry. CDW order in $NbSe_2$ monolayers induces a 3×3 reconstruction [20,53–56]. In a monolayer, we find two low-energy triangular reconstructions of the lattice [57], which are characterized by one of two structural distortions, classified as "hollow" or "filled," based on the distortion pattern of atoms in the Nb sublattice [58] (see Appendix B), and the hollow phase has the lowest overall energy of the two.

Both monolayer reconstructions are then used to create bilayer cells with different interlayer offsets of the CDW phase between the layers. The difference in DFT total energy between the normal (no reconstruction) phase and the hollow CDW phase on both layers, $\Delta E = E_{\mathrm{CDW}} - E_{\mathrm{normal}}$, is extracted to quantify the relative strength of the CDW phase between different structures. In agreement with the monolayer case, we find that structures with the hollow reconstruction on both layers are lowest in energy. We then calculate the relative strength of the CDW distortion at each of the 18 MX or XM (P) and 9 MM (AP) possible stacking configurations of the CDW in adjacent 3×3 reconstructed layers. Figure 6(a) shows these three unique structural configurations in the AP case, where only the Nb sublattice is shown to improve clarity (see Appendix B for additional figures showing the monolayer CDW reconstructions and the different interlayer configurations of these structures considered in this paper).

We observe a notable trend in this energy difference with interlayer disregistry, shown in the left (right) panel of Fig. 6(b) for the AP (P) bilayer. While it is possible to reach another low-energy mutual orientation of the two CDW distortions in each layer via a full dislocation in the AP bilayer, this is not possible for P bilayers, where shifting by a partial dislocation always leads to a higher-energy configuration. In a moiré superlattice, this suggests that the CDW order in adjacent layers will lock in inside a domain. Glide of the lattice by a partial or full screw dislocation across domain boundaries will rigidly shift the relative orientation of the CDW on each layer, and in order to attain a low-energy interlayer configuration, CDW discommensurations should nucleate at moiré dislocation boundaries [59,60], leading to CDW triplet domains in an AP moiré superlattice [61] and isolated CDW domains in a P moiré superlattice.

Conclusion. Multiscale relaxation and electronic structure calculations were performed on twisted-bilayer $NbSe_2$. Compared with semiconducting TMDs, monolayer $NbSe_2$ is relatively soft, and significant relaxation begins at slightly larger twist angles. The resulting domain structure for AP bilayers has hexagonal MM stacking domains with domain walls featuring XX stacking and seeds of $2H$ stacking in the alternating corners. The Fermi surface undergoes significant modulation across the moiré superlattice, with variation of the interlayer coupling at the K points on the order of 10–20 meV (25–55 meV) between different domains for an AP (P) bilayer. Notably, significant anisotropy in the interlayer coupling is observed along domain walls. For AP bilayers the interlayer coupling of metallic bands is strongest inside domains, in contrast to our finding regarding P bilayers. In P bilayers, the triangular MX or XM domains have smaller interlayer coupling of electron bands than along the triangular domain wall network.

A further observation arising from this work is that discommensurations [60] of the CDW phase should occur due to the rigid displacement of the relative orientation of the CDW in each layer which occurs at superlattice domain walls. CDW discommensurations are known to enhance the superconducting order in $TiSe_2$ [62–64]. This suggests a promising application for moiré superlattices in metallic TMDs systems as a method to control the CDW and, potentially, other order parameters. The potential for distinct modulation of interlayer hopping at each pocket, in addition to control of the CDW phase, along with anisotropic hopping at dislocation boundaries, suggests that marginally twisted $NbSe_2$ would be an interesting test system to further probe interlayer effects on correlated superconducting and CDW phases of the metallic TMDs [20].

Finally, we remark on possible implications of our results for Ising superconductivity in marginally twisted bilayers. At small angles, the interlayer coupling in both pockets across a significant area of the moiré supercell is of a similar magnitude to the MM bilayer, for both twisted AP and twisted P bilayers. In multilayer $NbSe_2$ [20] both the critical temperature T_c and in-plane magnetic field H_c of the superconducting transition show a significant dependence on the number of layers, suggesting the importance of interlayer electronic effects for the magnitude and form of the superconducting gap. If the breaking of spin-layer locking through increased interlayer hopping is the active mechanism in determining the superconducting transition temperature as a function of layer number, this suggests that the significant modulation of interlayer hopping by the moiré superstructure could be utilized to engineer superconductivity in specific domains of the superlattice. In an applied field, superconductivity would preferentially persist in regions of the moiré superlattice with smaller interlayer coupling, which are MX or XM domains (P bilayer) or domain walls and corners (AP bilayer).

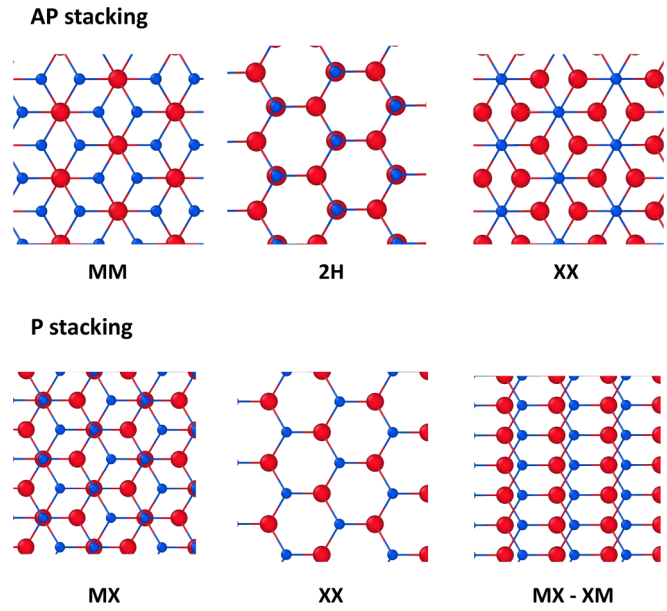

FIG. 7. Plan view of the main stacking orders occurring in twisted $NbSe_2$ domains.

TABLE II. DFT-calculated adhesion fit parameters.

C_1 (eV nm^2)	C_2 (eV nm^6)	C_3 (eV nm^{10})	A_1 (eV/nm^2)	A_2 (eV/nm^2)	ρ_1 (nm)	ρ_2 (nm)	d_0 (nm)	ε (eV/nm^4)
0.136	0.208	0.029	0.178	−0.016	0.051	0.042	0.66	214

Acknowledgment. This work was supported by the EC-FET European Graphene Flagship Core3 Project, EC-FET Quantum Flagship Project 2D-SIPC, EPSRC Grants No. EP/S030719/1 and No. EP/V007033/1, and a Lloyd's Register Foundation nanotechnology grant.

APPENDIX A: ADDITIONAL DFT CALCULATIONS AND PARAMETRIZATIONS

1. Stacking configurations

In Fig. 7 we provide illustrations of the main stacking orders occurring in twisted $NbSe_2$ domains: MM, $2H$, and XX for AP bilayers and MX, XM and XX for P bilayers.

2. DFT-calculated adhesion fit and elastic parameters

The DFT-calculated adhesion fit parameters C_1–C_3, A_1, A_2, ρ_1, ρ_2, d_0, and ε are given in Table II. The DFT-calculated lattice parameters a and c are provided in Table III along with the Young's modulus and Poisson's ratio.

3. DFT calculation of ferroelectric charge transfer

DFT calculations in mirror-reflected supercells demonstrate the presence of a ferroelectric charge transfer, resulting in an ≈ 11 meV potential energy drop between the layers; see Fig. 8.

4. Layer polarization

The left panels of Fig. 9 show the difference in the projection, onto the top and bottom layers, of DFT wave functions of the first and second metallic bands of an XM bilayer. The calculated interlayer hybridization with an additional layer-dependent term $\Delta_z\sigma_0\eta_z$, for $\Delta_z = 0$ meV and $\Delta_z = 20$ meV, is shown in the right panels.

5. Band structure and orbital projections

The electronic structure and orbital projections of the MM-AP bilayer are shown in Fig. 10. There is stronger interlayer splitting along the Γ-K and K-M directions, due to a higher proportion of d_z^2 orbitals.

TABLE III. DFT-calculated lattice parameters and elastic constants.

a (Å)	c (Å)	Young's modulus (N/m)	Poisson's ratio
3.45	12.74	77.92	0.334

6. Full expression for hybridization around the Γ and *K* pockets

We model spin and interlayer splitting at each pocket with a Hamiltonian

$$\mathcal{H}_i(\mathbf{p}) = \epsilon_i(\mathbf{p})\sigma_0\eta_0 d^\dagger_{\mathbf{p},i} d_{\mathbf{p},i} + \alpha_i(\mathbf{p})\sigma_0\eta_x + \beta_i(\mathbf{p})\sigma_z^a\eta_0. \quad \text{(A1)}$$

The interlayer term α varies with interlayer displacement between the layers, which also has periodic dependence on crystal momentum around a pocket,

$$\alpha_\Gamma(\mathbf{p}) = \bar{t}_\Gamma + t_{\Gamma,6}\cos(6\phi) + t_{\Gamma,2}\cos(2\phi) \quad \text{(A2)}$$

and

$$\alpha_K(\mathbf{p}) = \bar{t}_K + t_{K,3}\cos(3\phi) + t_{K,1}\cos(\phi). \quad \text{(A3)}$$

The $\cos(3\phi)$ and $\cos(6\phi)$ terms capture periodic dependence inside domains, while the $\cos(2\phi)$ and $\cos(\phi)$ terms are due to nematic distortion of pockets in the vicinity of dislocations. The parameters $\bar{t}_\Gamma$ and $\bar{t}_K$ are the average interlayer hybridization around a pocket. Spin-orbit terms are also included,

$$\beta_\Gamma(\mathbf{p}) = \lambda_\Gamma|\mathbf{p}|^3\cos(3\phi), \quad \text{(A4)}$$

such that spin splitting vanishes along the Γ-M directions, and with fixed splitting in the $K_\pm$ pockets,

$$\beta_K(\mathbf{p}) = \lambda_K. \quad \text{(A5)}$$

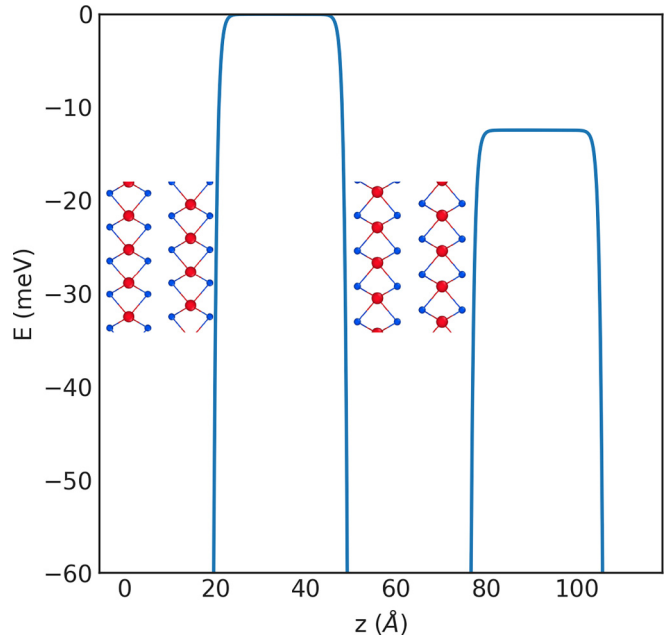

FIG. 8. Potential drop across a mirrored P bilayer shows ferroelectricity in P domains. There is a smaller ferroelectric charge transfer in comparison to semiconducting TMDs, $\Delta^P \approx 11$ meV.

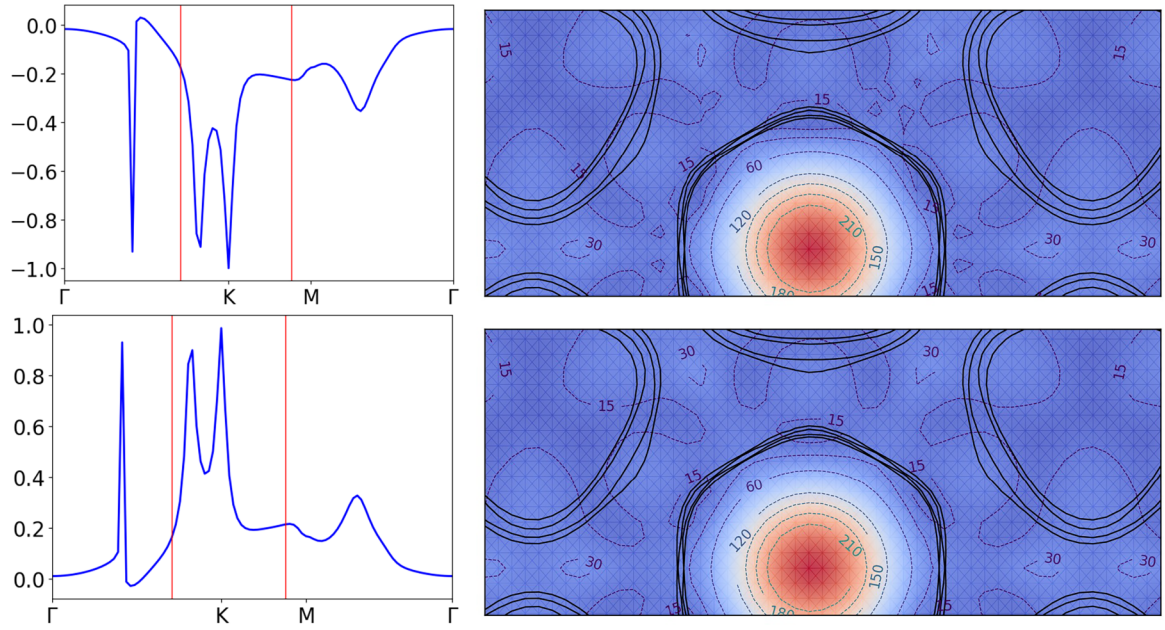

FIG. 9. Left: difference in the projection, onto the top and bottom layers, of DFT wave functions of the first metallic band (top panel) and second metallic band (bottom panel), of an XM bilayer. Right: calculated interlayer hybridization with an additional layer-dependent term $\Delta_z\sigma_0\eta_z$, for $\Delta_z = 0$ meV (same as main text; top panel) and $\Delta_z = 20$ meV (bottom panel).

7. Full hybridization parameters around the Γ and K pockets in domains and at domain boundaries

Tables IV and V provide the fits of α_Γ and α_K, respectively, at selected high-symmetry stackings for AP bilayers, in domains and at the domain wall (DW). Tables VI and VII give the fits of α_Γ and α_K, respectively, at selected high-symmetry stackings for P bilayers.

8. Fourier expansion of the hopping parameter across the moiré supercell

We have evaluated the average interlayer-hybridization term, $\bar{t}$, at individual pockets using DFT. We do this by performing band structure calculations along each of six individual high-symmetry lines in momentum space around each pocket, using fully relaxed cells (at fixed disregistry, i.e., fixed

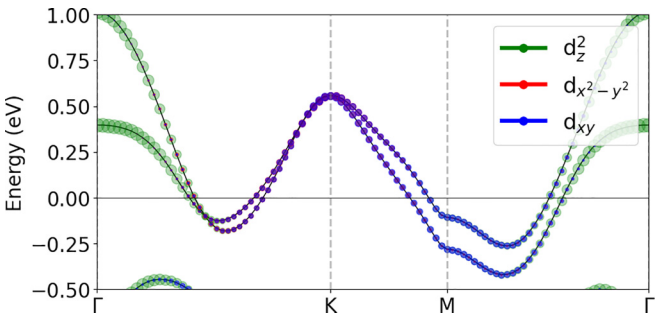

FIG. 10. Electronic structure and orbital projection of the MM-AP bilayer, where there is stronger interlayer splitting along the Γ-K and K-M directions, due to a higher proportion of d_z^2 orbitals.

TABLE IV. AP bilayer: Fit of α_Γ at selected high-symmetry stackings.

	$\bar{t}_\Gamma$ (meV)	$t_{\Gamma,6}$ (meV)	$t_{\Gamma,2}$ (meV)
$2H$	18.22	15.00	0.00
MM	52.73	21.00	0.00
XX	57.50	16.40	0.00
DW ($2H$-XX)	56.27	−4.33	24.54
DW (XX-MM)	47.05	3.78	−22.57

TABLE V. AP bilayer: Fit of α_K at selected high-symmetry stackings.

	$\bar{t}_K$ (meV)	$t_{K,6}$ (meV)	$t_{K,2}$ (meV)
$2H$	15.00	0.00	0.00
MM	21.00	0.00	0.00
XX	16.40	0.00	0.00
DW ($2H$-XX)	23.16	16.29	0.00
DW (XX-MM)	15.11	12.21	0.00

TABLE VI. P bilayer: Fit of α_Γ at selected high-symmetry stackings.

	$\bar{t}_\Gamma$ (meV)	$t_{\Gamma,3}$ (meV)	$t_{\Gamma,1}$ (meV)
MX	19.55	24.00	0.00
XX	66.46	52.95	0.00
DW (MX-XM)	34.94	0.00	−27.67

TABLE VII. P bilayer: Fit of α_K at selected high-symmetry stackings.

	$\bar{t}_K$ (meV)	$t_{K,3}$ (meV)	$t_{K,1}$ (meV)
MX	24.00	4.16	0.00
XX	52.95	10.49	0.00
DW (MX-XM)	11.62	13.63	21.75

TABLE VIII. Parameters of Fourier expansion of the interlayer coupling as a function of disregistry.

	V_0 (meV)	V_1 (meV)	ψ (deg)	r'
AP, Γ	36.55	3.88	7.44	XX
AP, K	14.90	1.20	112.00	XX
P, Γ	41.53	−4.97	59.80	MX
P, K	35.22	−3.84	59.70	MX

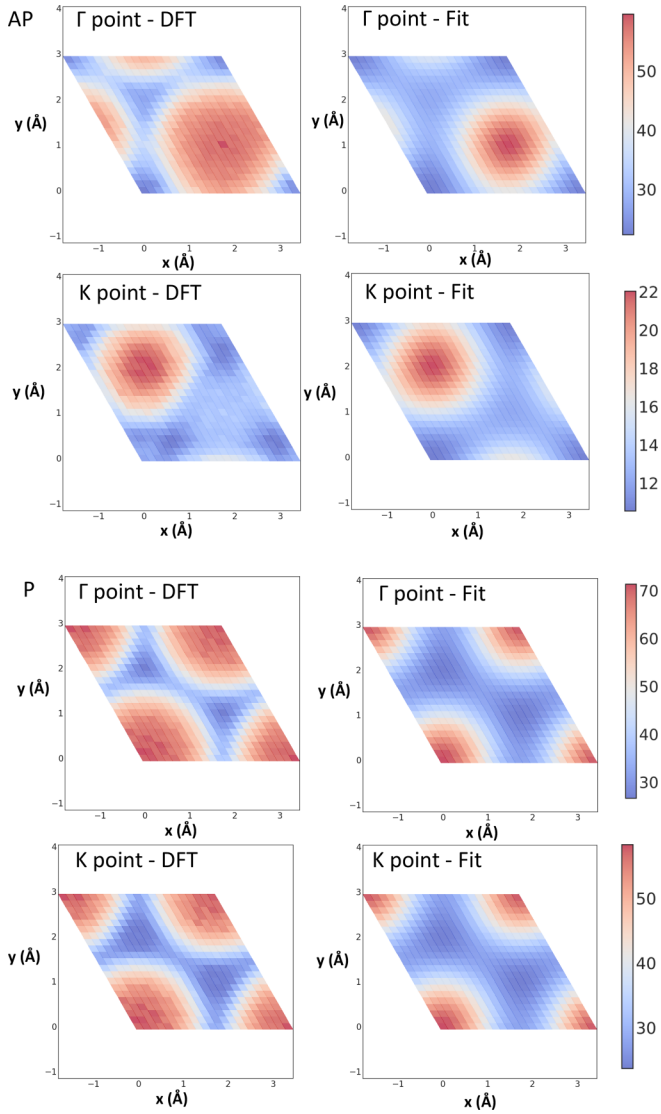

FIG. 11. DFT-calculated vs Fourier expansion of $\bar{t}_i$. All units are in meV.

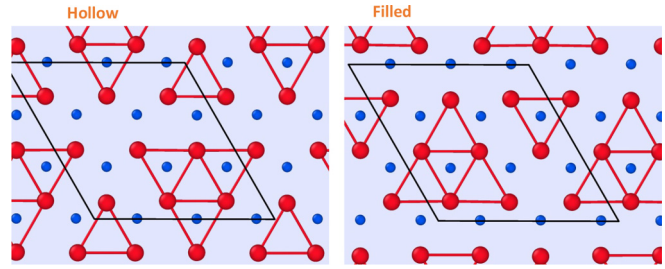

FIG. 12. Hollow and filled charge density wave structures with both Nb and Se sublattices shown. Nb distances are shown to demonstrate the degree of reconstruction due to the CDW phase.

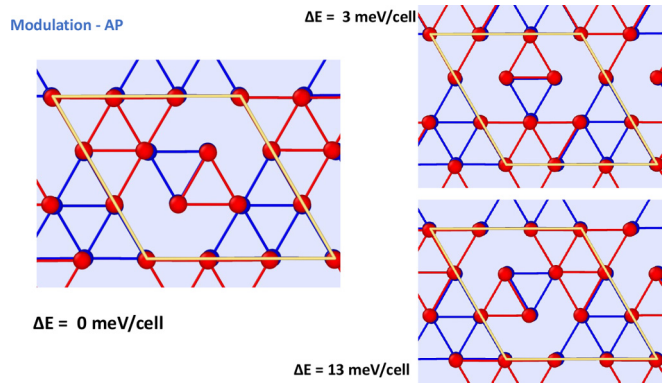

FIG. 13. Three distinct interlayer stacking configurations of hollow CDW distortions in AP-bilayers. The other nine stackings are 120° rotations of these structures.

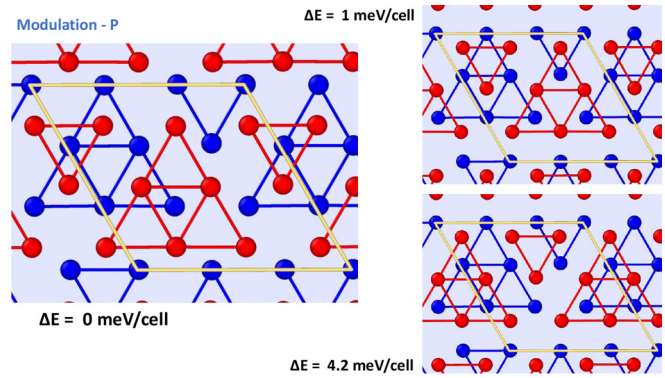

FIG. 14. Three distinct interlayer stacking configurations of hollow CDW distortions in P-bilayers. The other eighteen stackings are 120° rotations of these structures.

planar coordinates). We then average the value of $\alpha(\mathbf{p})$ at the Fermi level along these directions. The obtained DFT data (as a function of disregistry) are fitted to a Fourier expansion using the first star of reciprocal lattice vectors around the lattice site r',

$$\bar{t}_i(r_0) = V_0 + \sum_g V(g) e^{ig\cdot(r_0 - r')}, \tag{A6}$$

where the vectors g are the six TMD reciprocal lattice vectors in the first star, $g_n = \pm g_{1,2,3}$, and

$$V(g) = V^*(-g) = V_1 e^{i\psi}. \tag{A7}$$

The values of the parameters for the Fourier expansion, V_0, V_1, ψ, and r', are listed in Table VIII.

9. Fourier expansion of the average interlayer-hybridization parameter

In Fig. 11 we compare the DFT-calculated $\bar{t}_i$ with the Fourier expansion of $\bar{t}_i$ at the K and Γ points, for both AP and P bilayers.

APPENDIX B: CDW STRUCTURES

In this Appendix, we illustrate the hollow and filled charge density wave structures with both Nb and Se sublattices (Fig. 12) as well as the three distinct interlayer configurations of the hollow CDW for AP-stacked and P-stacked bilayers (Figs. 13 and 14).

[1] J. Sung, Y. Zhou, G. Scuri, V. Zólyomi, T. I. Andersen, H. Yoo, D. S. Wild, A. Y. Joe, R. J. Gelly, H. Heo, S. J. Magorrian, D. Bérubé, A. M. M. Valdivia, T. Taniguchi, K. Watanabe, M. D. Lukin, P. Kim, V. I. Fal'ko, and H. Park, Broken mirror symmetry in excitonic response of reconstructed domains in twisted $MoSe_2$/$MoSe_2$ bilayers, Nat. Nanotechnol. **15**, 750 (2020).

[2] D. Chen, Z. Lian, X. Huang, Y. Su, M. Rashetnia, L. Ma, L. Yan, M. Blei, L. Xiang, T. Taniguchi, K. Watanabe, S. Tongay, D. Smirnov, Z. Wang, C. Zhang, Y.-T. Cui, and S.-F. Shi, Excitonic insulator in a heterojunction moiré superlattice, Nat. Phys. **18**, 1171 (2022).

[3] H. Yoo, R. Engelke, S. Carr, S. Fang, K. Zhang, P. Cazeaux, S. H. Sung, R. Hovden, A. W. Tsen, T. Taniguchi, K. Watanabe, G.-C. Yi, M. Kim, M. Luskin, E. B. Tadmor, E. Kaxiras, and P. Kim, Atomic and electronic reconstruction at the van der Waals interface in twisted bilayer graphene, Nat. Mater. **18**, 448 (2019).

[4] A. Weston, Y. Zou, V. Enaldiev, A. Summerfield, N. Clark, V. Zólyomi, A. Graham, C. Yelgel, S. Magorrian, M. Zhou, J. Zultak, D. Hopkinson, A. Barinov, T. H. Bointon, A. Kretinin, N. R. Wilson, P. H. Beton, V. I. Fal'ko, S. J. Haigh, and R. Gorbachev, Atomic reconstruction in twisted bilayers of transition metal dichalcogenides, Nat. Nanotechnol. **15**, 592 (2020).

[5] M. R. Rosenberger, H.-J. Chuang, M. Phillips, V. P. Oleshko, K. M. McCreary, S. V. Sivaram, C. S. Hellberg, and B. T. Jonker, Twist angle-dependent atomic reconstruction and moiré patterns in transition metal dichalcogenide heterostructures, ACS Nano **14**, 4550 (2020).

[6] D. Halbertal, N. R. Finney, S. S. Sunku, A. Kerelsky, C. Rubio-Verdú, S. Shabani, L. Xian, S. Carr, S. Chen, C. Zhang, L. Wang, D. Gonzalez-Acevedo, A. S. McLeod, D. Rhodes, K. Watanabe, T. Taniguchi, E. Kaxiras, C. R. Dean, J. C. Hone, A. N. Pasupathy *et al.*, Moiré metrology of energy landscapes in van der Waals heterostructures, Nat. Commun. **12**, 242 (2021).

[7] L. J. McGilly, A. Kerelsky, N. R. Finney, K. Shapovalov, E.-M. Shih, A. Ghiotto, Y. Zeng, S. L. Moore, W. Wu, Y. Bai, K. Watanabe, T. Taniguchi, M. Stengel, L. Zhou, J. Hone, X. Zhu, D. N. Basov, C. Dean, C. E. Dreyer, and A. N. Pasupathy, Visualization of moiré superlattices, Nat. Nanotechnol. **15**, 580 (2020).

[8] S. Shabani, D. Halbertal, W. Wu, M. Chen, S. Liu, J. Hone, W. Yao, D. N. Basov, X. Zhu, and A. N. Pasupathy, Deep moiré potentials in twisted transition metal dichalcogenide bilayers, Nat. Phys. **17**, 720 (2021).

[9] D. Edelberg, H. Kumar, V. Shenoy, H. Ochoa, and A. N. Pasupathy, Tunable strain soliton networks confine electrons in van der Waals materials, Nat. Phys. **16**, 1097 (2020).

[10] R. Engelke, H. Yoo, S. Carr, K. Xu, P. Cazeaux, R. Allen, A. M. Valdivia, M. Luskin, E. Kaxiras, M. Kim, J. H. Han, and P. Kim, Topological nature of dislocation networks in two-dimensional moiré materials, Phys. Rev. B **107**, 125413 (2023).

[11] M. Van Winkle, I. M. Craig, S. Carr, M. Dandu, K. C. Bustillo, J. Ciston, C. Ophus, T. Taniguchi, K. Watanabe, A. Raja, S. M. Griffin, and D. K. Bediako, Rotational and dilational reconstruction in transition metal dichalcogenide moiré bilayers, Nat. Commun. **14**, 2989 (2023).

[12] N. P. Kazmierczak, M. V. Winkle, C. Ophus, K. C. Bustillo, S. Carr, H. G. Brown, J. Ciston, T. Taniguchi, K. Watanabe, and D. K. Bediako, Strain fields in twisted bilayer graphene, Nat. Mater. **20**, 956 (2021).

[13] V. V. Enaldiev, F. Ferreira, J. G. McHugh, and V. I. Fal'ko, Self-organized quantum dots in marginally twisted $MoSe_2$/WSe_2 and MoS_2/WS_2 bilayers, npj 2D Mater. Appl. **6**, 74 (2022).

[14] W.-Y. He, B. T. Zhou, J. J. He, N. F. Q. Yuan, T. Zhang, and K. T. Law, Magnetic field driven nodal topological superconductivity in monolayer transition metal dichalcogenides, Commun. Phys. **1**, 40 (2018).

[15] M. H. Fischer, M. Sigrist, and D. F. Agterberg, Superconductivity without inversion and time-reversal symmetries, Phys. Rev. Lett. **121**, 157003 (2018).

[16] L. Bawden, S. P. Cooil, F. Mazzola, J. M. Riley, L. J. Collins-McIntyre, V. Sunko, K. W. B. Hunvik, M. Leandersson, C. M. Polley, T. Balasubramanian, T. K. Kim, M. Hoesch, J. W. Wells, G. Balakrishnan, M. S. Bahramy, and P. D. C. King, Spin-valley locking in the normal state of a transition-metal dichalcogenide superconductor, Nat. Commun. **7**, 11711 (2016).

[17] S. C. de la Barrera, M. R. Sinko, D. P. Gopalan, N. Sivadas, K. L. Seyler, K. Watanabe, T. Taniguchi, A. W. Tsen, X. Xu, D. Xiao, and B. M. Hunt, Tuning Ising superconductivity with layer and spin-orbit coupling in two-dimensional transition-metal dichalcogenides, Nat. Commun. **9**, 1427 (2018).

[18] D. Wickramaratne, S. Khmelevskyi, D. F. Agterberg, and I. I. Mazin, Ising superconductivity and magnetism in $NbSe_2$, Phys. Rev. X **10**, 041003 (2020).

[19] M. D. Johannes, I. I. Mazin, and C. A. Howells, Fermi-surface nesting and the origin of the charge-density wave in $NbSe_2$, Phys. Rev. B **73**, 205102 (2006).

[20] X. Xi, Z. Wang, W. Zhao, J.-H. Park, K. T. Law, H. Berger, L. Forró, J. Shan, and K. F. Mak, Ising pairing in superconducting $NbSe_2$ atomic layers, Nat. Phys. **12**, 139 (2016).

[21] Y. Noat, J. A. Silva-Guillén, T. Cren, V. Cherkez, C. Brun, S. Pons, F. Debontridder, D. Roditchev, W. Sacks, L. Cario, P. Ordejón, A. García, and E. Canadell, Quasiparticle spectra of

$2H$–$NbSe_2$: Two-band superconductivity and the role of tunneling selectivity, Phys. Rev. B **92**, 134510 (2015).

[22] D. Lin, S. Li, J. Wen, H. Berger, L. Forró, H. Zhou, S. Jia, T. Taniguchi, K. Watanabe, X. Xi, and M. S. Bahramy, Patterns and driving forces of dimensionality-dependent charge density waves in $2H$-type transition metal dichalcogenides, Nat. Commun. **11**, 2406 (2020).

[23] M. Calandra, I. I. Mazin, and F. Mauri, Effect of dimensionality on the charge-density wave in few-layer $2H$-$NbSe_2$, Phys. Rev. B **80**, 241108(R) (2009).

[24] L. S. Farrar, A. Nevill, Z. J. Lim, G. Balakrishnan, S. Dale, and S. J. Bending, Superconducting quantum interference in twisted van der Waals heterostructures, Nano Lett. **21**, 6725 (2021).

[25] N. Yabuki, R. Moriya, M. Arai, Y. Sata, S. Morikawa, S. Masubuchi, and T. Machida, Supercurrent in van der Waals Josephson junction, Nat. Commun. **7**, 10616 (2016).

[26] Y. Zhang, C. Felser, and L. Fu, Moiré metal for catalysis, arXiv:2111.03058.

[27] P. Giannozzi, S. Baroni, N. Bonini, M. Calandra, R. Car, C. Cavazzoni, D. Ceresoli, G. L. Chiarotti, M. Cococcioni, I. Dabo, A. D. Corso, S. de Gironcoli, S. Fabris, G. Fratesi, R. Gebauer, U. Gerstmann, C. Gougoussis, A. Kokalj, M. Lazzeri, L. Martin-Samos *et al.*, QUANTUM ESPRESSO: a modular and open-source software project for quantum simulations of materials, J. Phys.: Condens. Matter **21**, 395502 (2009).

[28] P. Giannozzi, O. Andreussi, T. Brumme, O. Bunau, M. B. Nardelli, M. Calandra, R. Car, C. Cavazzoni, D. Ceresoli, M. Cococcioni, N. Colonna, I. Carnimeo, A. D. Corso, S. de Gironcoli, P. Delugas, R. A. DiStasio, A. Ferretti, A. Floris, G. Fratesi, G. Fugallo *et al.*, Advanced capabilities for materials modelling with Quantum ESPRESSO, J. Phys.: Condens. Matter **29**, 465901 (2017).

[29] K. F. Garrity, J. W. Bennett, K. M. Rabe, and D. Vanderbilt, Pseudopotentials for high-throughput DFT calculations, Comput. Mater. Sci. **81**, 446 (2014).

[30] J. P. Perdew, K. Burke, and M. Ernzerhof, Generalized gradient approximation made simple, Phys. Rev. Lett. **77**, 3865 (1996).

[31] H. J. Monkhorst and J. D. Pack, Special points for Brillouin-zone integrations, Phys. Rev. B **13**, 5188 (1976).

[32] T. Thonhauser, V. R. Cooper, S. Li, A. Puzder, P. Hyldgaard, and D. C. Langreth, Van der Waals density functional: Self-consistent potential and the nature of the van der Waals bond, Phys. Rev. B **76**, 125112 (2007).

[33] T. Thonhauser, S. Zuluaga, C. A. Arter, K. Berland, E. Schröder, and P. Hyldgaard, Spin signature of nonlocal correlation binding in metal-organic frameworks, Phys. Rev. Lett. **115**, 136402 (2015).

[34] K. Berland, V. R. Cooper, K. Lee, E. Schröder, T. Thonhauser, P. Hyldgaard, and B. I. Lundqvist, van der Waals forces in density functional theory: a review of the vdW-DF method, Rep. Prog. Phys. **78**, 066501 (2015).

[35] D. C. Langreth, B. I. Lundqvist, S. D. Chakarova-Käck, V. R. Cooper, M. Dion, P. Hyldgaard, A. Kelkkanen, J. Kleis, L. Kong, S. Li, P. G. Moses, E. Murray, A. Puzder, H. Rydberg, E. Schröder, and T. Thonhauser, A density functional for sparse matter, J. Phys.: Condens. Matter **21**, 084203 (2009).

[36] A. Meerschaut and C. Deudon, Crystal structure studies of the 3R-$Nb_{1.09}S_2$ and the 2H-$NbSe_2$ compounds: correlation between nonstoichiometry and stacking type (= polytypism), Mater. Res. Bull. **36**, 1721 (2001).

[37] R. Kershaw, M. Vlasse, and A. Wold, The preparation of and electrical properties of niobium selenide and tungsten selenide, Inorg. Chem. **6**, 1599 (1967).

[38] J. Feldman, Elastic constants of 2H-MoS_2 and 2H-$NbSe_2$ extracted from measured dispersion curves and linear compressibilities, J. Phys. Chem. Solids **37**, 1141 (1976).

[39] X. Lv, W. Wei, Q. Sun, B. Huang, and Y. Dai, A first-principles study of $NbSe_2$ monolayer as anode materials for rechargeable lithium-ion and sodium-ion batteries, J. Phys. D: Appl. Phys. **50**, 235501 (2017).

[40] M. Gardos, On the elastic constants of thin solid lubricant films, Tribol. Ser. **17**, 3 (1990).

[41] H. Wang, X. Huang, J. Lin, J. Cui, Y. Chen, C. Zhu, F. Liu, Q. Zeng, J. Zhou, P. Yu, X. Wang, H. He, S. H. Tsang, W. Gao, K. Suenaga, F. Ma, C. Yang, L. Lu, T. Yu, E. H. T. Teo *et al.*, High-quality monolayer superconductor $NbSe_2$ grown by chemical vapour deposition, Nat. Commun. **8**, 394 (2017).

[42] T. Valla, A. V. Fedorov, P. D. Johnson, P.-A. Glans, C. McGuinness, K. E. Smith, E. Y. Andrei, and H. Berger, Quasiparticle spectra, charge-density waves, superconductivity, and electron-phonon coupling in 2H–$NbSe_2$, Phys. Rev. Lett. **92**, 086401 (2004).

[43] Y. Nakata, K. Sugawara, S. Ichinokura, Y. Okada, T. Hitosugi, T. Koretsune, K. Ueno, S. Hasegawa, T. Takahashi, and T. Sato, Anisotropic band splitting in monolayer $NbSe_2$: implications for superconductivity and charge density wave, npj 2D Mater. Appl. **2**, 12 (2018).

[44] D. J. Rahn, S. Hellmann, M. Kalläne, C. Sohrt, T. K. Kim, L. Kipp, and K. Rossnagel, Gaps and kinks in the electronic structure of the superconductor $2H$-$NbSe_2$ from angle-resolved photoemission at 1 K, Phys. Rev. B **85**, 224532 (2012).

[45] S. V. Borisenko, A. A. Kordyuk, V. B. Zabolotnyy, D. S. Inosov, D. Evtushinsky, B. Büchner, A. N. Yaresko, A. Varykhalov, R. Follath, W. Eberhardt, L. Patthey, and H. Berger, Two energy gaps and Fermi-surface "arcs" in $NbSe_2$, Phys. Rev. Lett. **102**, 166402 (2009).

[46] V. V. Enaldiev, V. Zólyomi, C. Yelgel, S. J. Magorrian, and V. I. Fal'ko, Stacking domains and dislocation networks in marginally twisted bilayers of transition metal dichalcogenides, Phys. Rev. Lett. **124**, 206101 (2020).

[47] R. He, J. van Baren, J.-A. Yan, X. Xi, Z. Ye, G. Ye, I.-H. Lu, S. M. Leong, and C. H. Lui, Interlayer breathing and shear modes in $NbSe_2$ atomic layers, 2D Mater. **3**, 031008 (2016).

[48] The values of critical angles θ_{P}^{*} and θ_{AP}^{*} result from the equality of the gain from the formation of domains to the costs of the domain wall network.

[49] A. Kormányos, G. Burkard, M. Gmitra, J. Fabian, V. Zólyomi, N. D. Drummond, and V. Fal'ko, Corrigendum: k.p theory for two-dimensional transition metal dichalcogenide semiconductors, 2D Mater. **2**, 049501 (2015).

[50] D. Shaffer, J. Kang, F. J. Burnell, and R. M. Fernandes, Crystalline nodal topological superconductivity and Bogolyubov Fermi surfaces in monolayer $NbSe_2$, Phys. Rev. B **101**, 224503 (2020).

[51] F. Flicker, The geometry and topology of charge-ordered quantum fields in low-dimensional systems, Ph.D. thesis, University of Bristol, 2015.

[52] F. Ferreira, V. V. Enaldiev, V. I. Fal'ko, and S. J. Magorrian, Weak ferroelectric charge transfer in layer-asymmetric bilayers of 2D semiconductors, Sci. Rep. **11**, 13422 (2021).

[53] M. M. Ugeda, A. J. Bradley, Y. Zhang, S. Onishi, Y. Chen, W. Ruan, C. Ojeda-Aristizabal, H. Ryu, M. T. Edmonds, H.-Z. Tsai, A. Riss, S.-K. Mo, D. Lee, A. Zettl, Z. Hussain, Z.-X. Shen, and M. F. Crommie, Characterization of collective ground states in single-layer $NbSe_2$, Nat. Phys. **12**, 92 (2016).

[54] J. Dai, E. Calleja, J. Alldredge, X. Zhu, L. Li, W. Lu, Y. Sun, T. Wolf, H. Berger, and K. McElroy, Microscopic evidence for strong periodic lattice distortion in two-dimensional charge-density wave systems, Phys. Rev. B **89**, 165140 (2014).

[55] C. J. Arguello, S. P. Chockalingam, E. P. Rosenthal, L. Zhao, C. Gutiérrez, J. H. Kang, W. C. Chung, R. M. Fernandes, S. Jia, A. J. Millis, R. J. Cava, and A. N. Pasupathy, Visualizing the charge density wave transition in $2H$-$NbSe_2$ in real space, Phys. Rev. B **89**, 235115 (2014).

[56] J. Á. Silva-Guillén, P. Ordejón, F. Guinea, and E. Canadell, Electronic structure of $2H$-$NbSe_2$ single-layers in the CDW state, 2D Mater. **3**, 035028 (2016).

[57] B. Guster, C. Rubio-Verdú, R. Robles, J. Zaldívar, P. Dreher, M. Pruneda, J. Á. Silva-Guillén, D.-J. Choi, J. I. Pascual, M. M. Ugeda, P. Ordejón, and E. Canadell, Coexistence of elastic modulations in the charge density wave state of $2H$-$NbSe_2$, Nano Lett. **19**, 3027 (2019).

[58] C.-S. Lian, C. Si, and W. Duan, Unveiling charge-density wave, superconductivity, and their competitive nature in two-dimensional $NbSe_2$, Nano Lett. **18**, 2924 (2018).

[59] S. Lim, J. Kim, C. Won, and S.-W. Cheong, Atomic-scale observation of topological vortices in the incommensurate charge density wave of 2H-$TaSe_2$, Nano Lett. **20**, 4801 (2020).

[60] W. L. McMillan, Theory of discommensurations and the commensurate-incommensurate charge-density-wave phase transition, Phys. Rev. B **14**, 1496 (1976).

[61] Z. A. H. Goodwin and V. I. Fal'ko, Moiré modulation of charge density waves, J. Phys.: Condens. Matter **34**, 494001 (2022).

[62] C. Chen, L. Su, A. H. Castro Neto, and V. M. Pereira, Discommensuration-driven superconductivity in the charge density wave phases of transition-metal dichalcogenides, Phys. Rev. B **99**, 121108(R) (2019).

[63] Y. I. Joe, X. M. Chen, P. Ghaemi, K. D. Finkelstein, G. A. de la Peña, Y. Gan, J. C. T. Lee, S. Yuan, J. Geck, G. J. MacDougall, T. C. Chiang, S. L. Cooper, E. Fradkin, and P. Abbamonte, Emergence of charge density wave domain walls above the superconducting dome in $1T$-$TiSe_2$, Nat. Phys. **10**, 421 (2014).

[64] B. Leridon, S. Caprara, J. Vanacken, V. V. Moshchalkov, B. Vignolle, R. Porwal, R. C. Budhani, A. Attanasi, M. Grilli, and J. Lorenzana, Protected superconductivity at the boundaries of charge-density-wave domains, New J. Phys. **22**, 073025 (2020).